

Fast and sensitive multivalent spatial pattern-recognition for circular RNA detection

Received: 21 May 2024

Accepted: 9 December 2024

Published online: 30 December 2024

 Check for updates

Zhixin Zhou^{1,7}, Bing Han^{2,7}, Yu Wang², Nina Lin¹, Zhongqiu Zhou², Yuan Zhang², Ying Bai², Ling Shen², Yanfei Shen³, Yuanjian Zhang¹✉ & Honghong Yao^{2,4,5,6}✉

While circular RNAs (circRNAs) exhibit lower abundance compared to corresponding linear RNAs, they demonstrate potent biological functions. Nevertheless, challenges arise from the low concentration and distinctive structural features of circRNAs, rendering existing methods operationally intricate and less sensitive. Here, we engineer an intelligent tetrahedral DNA framework (TDF) possessing precise spatial pattern-recognition properties with exceptional sensing speed and sensitivity for circRNAs. The signal output of TDF sensor occurs only when multivalent spatial pattern-recognition of a circRNA in unamplified samples. Using this sensor, we visualize the real-time response of endogenous circRNA expression in vitro neuronal cells and in vivo brain between pre-stroke and post-stroke male mice, identify the patients with acute ischemic stroke in clinical samples, as well as track the delivery of circRNA in photochromic stroked animal model. Thus, the TDF sensor provides a fast and sensitive tool for the detection of circRNA abundance in both physiological and pathophysiological conditions.

Circular RNAs (circRNAs), formed by back-splicing of linear RNAs, are single-stranded, covalently closed RNA molecules prevalent across diverse species, spanning from viruses to mammals^{1,2}. CircRNAs not only have emerged as crucial and distinctive regulators in life processes but also possess distinct advantages in the development and application of clinical diagnostic markers³. This is attributed to the high stability and conserved natural expression specificity of circRNAs⁴. Conducting highly precise analyses of circRNAs in bulk biofluids and tissues is critically important for advancing biological research, enhancing precision medicine, and enabling early-stage disease diagnoses⁵. Nonetheless, traditional methods like quantitative reverse-transcription polymerase chain reaction (RT-qPCR) and

fluorescence in situ hybridization (FISH) demand skilled personnel, specialized laboratories and equipment, and extended processing times exceeding 24 h. Hence, the fast and sensitive detection of circRNAs remains challenging in the fields of chemical and biological sciences due to ultralow abundance of many diseases-associated circRNAs⁶. This challenge is becoming increasingly pressing, especially in the visualization of circRNAs in living cells, detecting circRNA level in clinical samples, and tracking exogenous circRNAs in vivo.

Detecting circRNAs in live cells presents greater challenges compared to linear RNAs, primarily because probe design is confined to the region of the back-splice junction (BSJ), which is the only sequence that permits clear identification of the circular form^{7,8}. Furthermore, the

¹School of Chemistry and Chemical Engineering, Jiangsu Provincial Key Laboratory of Critical Care Medicine, Southeast University, Nanjing, China.

²Department of Pharmacology, Jiangsu Provincial Key Laboratory of Critical Care Medicine, School of Medicine, Southeast University, Nanjing, China. ³School of Medicine, Southeast University, Nanjing, China. ⁴Co-innovation Center of Neuroregeneration, Nantong University, Nantong, China. ⁵Institute of Life Sciences, Key Laboratory of Developmental Genes and Human Disease, Southeast University, Nanjing, China. ⁶Center for Global Health, School of Public Health, Nanjing Medical University, Nanjing, China. ⁷These authors contributed equally: Zhixin Zhou, Bing Han. ✉e-mail: yuanjian.zhang@seu.edu.cn; yaohh@seu.edu.cn

presence of ultralong sequences, competing secondary structures, interactions with RNA-binding proteins, or the sequestration of RNA into granules create obstacle that hinder probe binding to the target sequence, resulting in reduced hybridization kinetics, low binding efficiency, and increased nonspecific interactions⁷. Inspired by the natural structures, in which the octopus has evolved eight flexible arms with adhesive suckers for preying to maximize the touch and capture efficiency of flowing targets, and the multivalent interaction can support tight binding of virus to host cells facilitated by spatially patterned antigens on viral surfaces^{9–12}, we sought to design an intelligent nanorobotic with precise, multivalent spatial pattern-recognizing properties to enhance the capture efficiency and binding affinity toward circRNAs. The spatial organization with molecular precision and superior programmability of DNA nanostructure provides a powerful tool to organize spacing, valency, and spatial arrangements of various molecules including nucleic acids, peptides, and proteins, for material and medical sciences^{13–16}. Furthermore, the typical nanoscale size, biocompatible nature, and structural stability of DNA nanostructure offer advantages, including effective permeation into live cells without the time-consuming and complex transfection process, no obvious cytotoxicity, and high biostability in various types of living cells^{17–19}.

Herein, we present a design strategy that employs a tetrahedral DNA framework (TDF) for the selective recognition and high-affinity capture of intact circRNAs. The TDF interacts with circRNAs via pattern-matching and multivalent interaction, thus resulting in significantly improved hybridization kinetics (within 1 min) and hybridization efficiency. Using the sensitive probe, the DNA sensors demonstrate high sensitivity and high selectivity. The logic behind leveraging the high cellular uptake efficiency of TDF sensors and their high binding affinity towards circRNAs is to facilitate various applications. By utilizing the TDF sensors, circRNAs can be directly visualized in living cells, freely moving animals, and tissue sections. This direct visualization provides valuable insights into circRNA localization and dynamics within biological systems. Additionally, TDF sensors enable the detection of circRNA levels in total RNAs extracted from clinical samples, facilitating the study of circRNA expression profiles in disease states or physiological conditions. Furthermore, aside from labeling endogenous circRNAs, the structure also allows for the tracking of exogenous circRNA in vivo. This capability is particularly valuable for investigating the behavior and fate of exogenously introduced circRNAs, utilizing extracellular vesicle delivery mechanisms for potential therapeutic applications or studying intercellular communication mediated by circRNAs. Our approach to designing the molecular platform aims to provide valuable tools for the tracking and quantification of circRNA with improved sensitivity, specificity, and ultrafast speed. These are essential for achieving a comprehensive understanding of the roles and mechanisms of circRNAs in diverse biological processes, as well as for exploring their potential applications in clinical diagnostics and therapeutics.

Results

Development and characterization of the TDF-based circSCMH1 sensing

Our previous study demonstrated that circular RNA *SCMH1*, circSCMH1 (6, 7, 8) (hereafter referred to as circSCMH1), was highly expressed in the brain, but was significantly downregulated in acute ischemic stroke (AIS) patients, thus offering a diagnostic and therapeutic biomarker for ischemic stroke²⁰. Thus, circSCMH1 is selected as a model target, which is originated from 6, 7, and 8 exons of the *SCMH1* gene (Fig. 1A). The predicted conformation of the circSCMH1 by RNAfold software revealed a complicated intrinsic secondary structure, which would prevent hybridization process, and thus lead to low hybridization kinetic and weak affinity (Figs. 1B and S1). To detect circRNAs with high sensitivity and selectivity, we have designed TDF

sensor, which is composed of three functional components: (i) To enhance the binding affinity and eliminate non-specific off-target effects, three target sequences, BSJ and another two splice junctions of circSCMH1 were selected (Fig. S1). (ii) Based on the structure of the circSCMH1, the possible distance between two neighboring target sites is estimated to be ca. 10–14 nm. Thus, the TDF with side length of 37 base pairs (≈12.6 nm) was designed with triangular units to match the pattern and spacing of the three target sequences of circSCMH1. (iii) Three probe sites recognizing the three targeting sequences of circRNAs are fluorophore-labeled but their fluorescence is quenched by BHQ-modified DNA (Q) that hybridizes with the probes. The TDF was functionalized for detection of circSCMH1 by hybridizing these three fluorophore/quencher-functionalized probes at their edges to form multivalent TDF sensor that geometrically matched and targeted circSCMH1 (Fig. 1C). In the presence of circSCMH1, the binding between the TDF sensor and the target sequences will displace the quencher strands, leading to the spatial separation of the quencher from the fluorophore and thus the recovery of the fluorescence signal of fluorophore. These probes attached on the TDF provide local structural flexibility to allow for binding of circSCMH1 under various solution conditions. The TDF was constructed by a simple thermal annealing process of eleven appropriately designed oligonucleotides (Fig. S2A and Table S1). The formation of the intact TDF sensor was characterized by 4% agarose gel electrophoresis (Fig. S2B), which was proved to be a reliable tool for evaluating structure and yield of DNA nanostructure^{10,18}. As shown in Fig. S2B, the stepwise increase in the molecular weight of the structures with the stepwise addition of component strand reveals the expected assembly behaviour of TDF with high yield. Atomic force microscopy (AFM) imaging further confirmed the formation of the TDF with triangle shape and size of 13.8 ± 2.2 nm (Figs. 1D, E and S2C), close to the theoretical value ca. 12.6 nm. It should be noted that AFM may show overall shape of TDF structure but cannot fully reveal the details of the TDF structure owing to the limited resolution.

To evaluate the feasibility of the proposed TDF in detecting the circSCMH1, HEK293T cells were transfected with circSCMH1 plasmids to induce the overexpression of circSCMH1 without the change of the linear *SCMH1* mRNA expression (Fig. S3). The total RNA extracted from the cells was analyzed by the TDF sensor directly. As shown in Fig. 1F, TDF sensor unambiguously distinguished the overexpression of circSCMH1 from the vector group. And the fluorescence signal of the TDF sensor gradually enhances with the increased concentration of circSCMH1 (Fig. 1G). As quantification of circSCMH1 copies in the total RNA extraction through qPCR, it was revealed that the TDF sensor could detect concentrations as low as 100 copies/nL of circSCMH1 isolating from transfected cells. We then characterized the specificity and kinetic of the TDF sensor. No measurable response was produced by any other microRNAs and another circular RNA (Fig. 1H), confirming the specificity of TDF for binding of specific circSCMH1. We then observed fast DNA hybridization kinetics and obtained a saturated signal within 60 s for the TDF sensor, implying the strong binding avidity between circSCMH1 (1 pM) and TDF sensor. However, under the same concentration, neither the single selective BSJ region nor the three short synthetic fragment RNAs (comprising one BSJ region and two splicing sites) of circSCMH1 resulted in detectable fluorescence changes (Figs. 1I and S4A, B). As the concentration of this short synthetic RNAs increase to 300 nM, relatively slow hybridization kinetics and the saturated signals were observed within 400 s (Figs. 1I and S4A, B). These TDF sensors bond strongly to circRNAs through multivalent interactions with enhanced sensing speed and sensitivity. However, TDF probes targeted linear RNAs in a one-on-one manner, resulting in weaker binding strength and less detection sensitivity compared with the multivalent interaction manner. Our findings highlighted the importance of multivalent spatial pattern-recognition for enhancing the biorecognition efficiency.

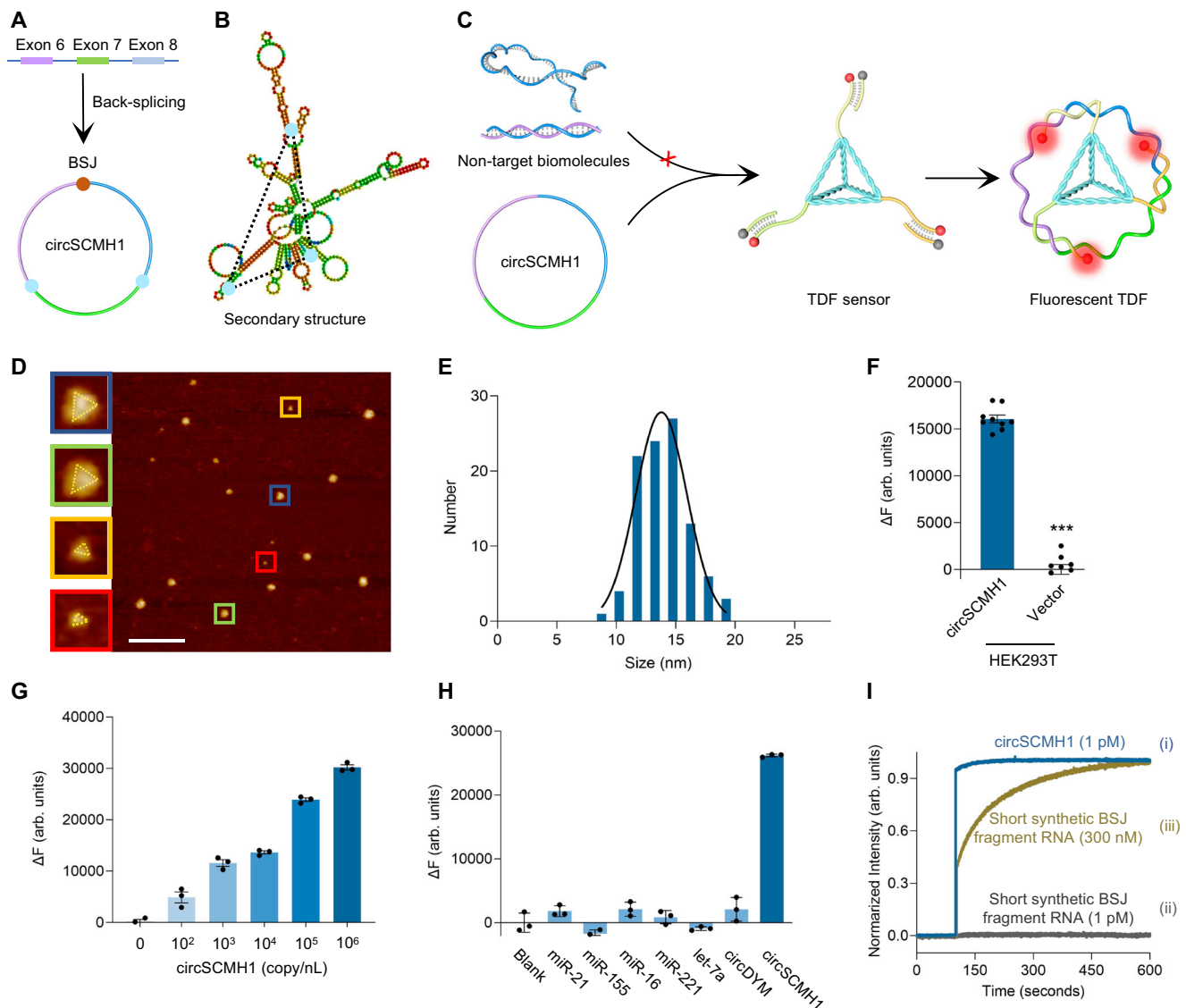


Fig. 1 | Development and characterization of the TDF sensor. **A** CircSCMH1 derived from the exon 6, 7, and 8 of the *SCMH1* gene. **B** Predicted circSCMH1 structure calculated by RNAfold software. **C** Schematic illustration for sensing mechanism of TDF sensor. **D** AFM characterization demonstrating the successful formation of TDF. Scale bar, 100 nm. Experiments were repeated independently three times with similar results. **E** The average size of the TDF sensor derived from AFM image. **F** Fluorescence intensity of TDF sensor upon the addition of RNA extraction from circSCMH1 plasmid-transfected HEK293T and vector-transfected HEK293T cells. Data are presented as mean \pm SEM, $n = 9$ different measurements/group. *** $P < 0.001$ versus Con group using unpaired two-tailed

Student's t test. **G** Fluorescence intensity of TDF probe upon addition of different concentrations of circSCMH1 from plasmid-transfected HEK293T cells. Data are presented as mean \pm SEM, $n = 3$ different measurements/group. **H** Fluorescence changes in response to the indicated compounds. Data are presented as mean \pm SEM, $n = 3$ different measurements/group. **I** Fluorescence kinetic of TDF sensor upon addition of circSCMH1 (1 pM) isolated from transfected cells (i), short synthetic BSJ fragment RNA (1 pM) (ii), and short synthetic BSJ fragment RNA (300 nM) (iii). BSJ back-splice junction, arb. units arbitrary units; Source data are provided as a Source Data file.

Multivalency and spatial pattern on the sensitivity of TDF sensor

Next, to evaluate whether spatial pattern matching of TDF sensor was crucial for sensing capabilities, four different TDFs with different size, namely, TDF with side length of 17 base pairs (TDF-17, 5.8 nm spacing), 26 base pairs (TDF-26, 8.8 nm spacing), 37 base pairs (TDF-37, 12.6 nm spacing), and 47 base pairs (TDF-47, 15.5 nm spacing) were designed (Fig. 2A and Table S1) and then characterized using 4% agarose gel electrophoresis (Figs. S2B and S5A–C). These TDFs were functionalized with three identical probes as recognition elements for circSCMH1. The TDF-37 exhibited the best sensing capacity for detecting circSCMH1 among these different size TDF sensors in isolated RNAs (Fig. 2B) as well as in cells and brain slices (Fig. S6A–D). In addition, to examine whether any other products during synthesis of TDF sensor will affect the detection of circSCMH1, the TDF sensor was purified by

using ultrafiltration device. No significant difference in recognition signal for circSCMH1 was observed before and after the purification of TDF sensor, suggesting that the potential byproduct could not affect the detection of circSCMH1 (Fig. S7A). Taken together, this finding indicated that the spatial pattern recognition was critical for sensing circSCMH1 since a small mismatch of geometry, under the identical ligand valency, resulted in significantly reduced sensing performance.

Furthermore, to explore the effect of multivalent interactions in promoting the detection sensitivity of the TDF sensor for circSCMH1, we systematically performed detection assays of TDF sensors with different probe sites, i.e., TDF-1 with single probe site for BSJ, TDF-2 with two probe sites, and TDF-37 with three probe sites. As displayed in Fig. 2C, a significant decrease in detection sensitivity was observed

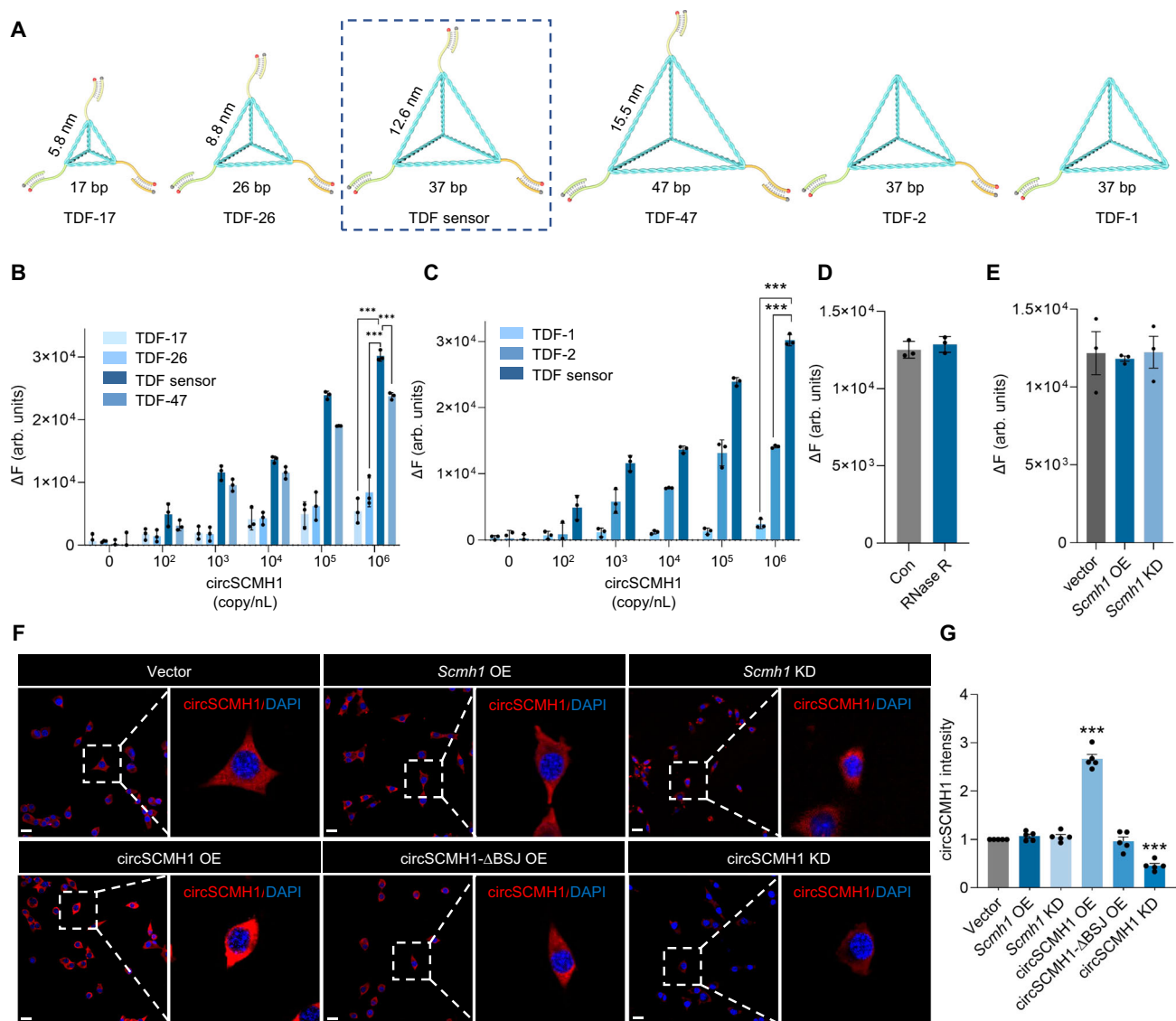


Fig. 2 | Effect of multivalency and spatial pattern on the sensitivity of TDF sensor. **A** Schematic showing the design of TDF with side length of 17 base pairs (TDF-17), 26 base pairs (TDF-26), TDF sensor, 47 base pairs (TDF-47), TDF-1 with single probe site for BSJ, and TDF-2 with two probe sites. **B** Fluorescence intensity of TDF-17, TDF-26, TDF-47, and TDF sensor upon addition of different concentrations of circSCMH1 from plasmid-transfected HEK293T cells. Data are presented as mean \pm SEM, $n = 3$ different measurements/group. *** $P < 0.001$ versus TDF sensor group using unpaired two-tailed Student's t test. **C** Fluorescence intensity of TDF-1, TDF-2, and TDF sensor upon addition of different concentrations of circSCMH1 from plasmid-transfected HEK293T cells. Data are presented as mean \pm SEM, $n = 3$ different measurements/group. *** $P < 0.001$ versus TDF sensor group using unpaired two-tailed Student's t test. **D** Fluorescence intensity of TDF sensor upon addition of total RNAs and RNase R-treated total RNAs from HT-22 cells. Data are

presented as mean \pm SEM, $n = 3$ different measurements/group. $P = 0.4681$ versus Con group using unpaired two-tailed Student's t test. **E** Fluorescence intensity of circSCMH1 from HT-22 cells treated with overexpression (OE) and knockdown (KD) of linear *Scmh1* mRNAs. Data are presented as mean \pm SEM, $n = 3$ different biological replicates/group. $P = 0.9642$ (*Scmh1* OE) and $P = 0.9657$ (*Scmh1* KD) versus Con group using one-way ANOVA followed by Holm-Sidak post hoc multiple comparison test. **F** Images of circSCMH1 in HT-22 cells after Vector (negative control), *Scmh1* OE, *Scmh1* KD, circSCMH1 OE, circSCMH1- Δ BSJ OE and circSCMH1 KD treatment. $n = 5$ biological replicates/group. Scale bar, 20 μ m. **G** Quantification of circSCMH1 intensity in HT-22 cells. Data are presented as mean \pm SEM. *** $P < 0.001$ versus Vector group using one-way ANOVA followed by Holm-Sidak post hoc multiple comparison test. arb. units, arbitrary units; Con, control; BSJ, back-splice junction. Source data are provided as a Source Data file.

with decreasing probe sites, clearly demonstrating the advantage of multivalent interactions in enhancing binding avidity between circSCMH1 and TDF-37. Additionally, we synthesized a TDF with two flanking exon-exon probes lacking fluorophore/quencher pairs, its signal intensity for detecting circRNA was significantly reduced compared to the TDF-37 (Fig. S7B, C), suggesting the superiority of including fluorophore/quencher pairs in the two flanking exon-exon probes for signal amplification. Taken together, due to complicated secondary conformation generated by the long sequence of circSCMH1, the multivalent TDF-37 with precise spatial pattern-recognition properties is able to enhance the recognition ratio with

circSCMH1. In the present study, unless otherwise specified, TDF-37 was used as the default TDF sensor in the following studies.

Usually, probe recognition of circRNAs is most susceptible to interference from homologous linear sequences. Thus, RNase R treatment was used as a stringent validation approach by selectively degrading linear transcripts⁸. RNase R treatment did not significantly affect the TDF sensor's recognition signal for circSCMH1 from HT-22 cells (Figs. 2D and S8A). Further study indicated that the sensor was highly specific to the circular form as evidenced by the fact that TDF sensor's recognition signal and DNA hybridization kinetics for the isolated circSCMH1 from HT-22 cells remained unchanged despite the

overexpression and knockdown of linear *Scmh1* mRNA (Figs. 2E and S8B–G). This finding was confirmed in the HT-22 cells with the TDF sensor followed by detection of circSCMH1 under the microscope (Fig. 2F). Next, in order to assess the impact of mutations at the binding sites, we constructed a plasmid that expressed a mutant form of circSCMH1 lacking the BSJ sequence (circSCMH1-ΔBSJ) by removing 18 nucleotides upstream and downstream of the BSJ. There was no significant difference of the fluorescence signal in the cells transfected with the circSCMH1-ΔBSJ-expressing plasmid compared with that of cells transfected with an empty vector. However, the fluorescence signal was significantly increased in HT-22 cells with overexpressing the wild-type circSCMH1 and was reduced in circSCMH1-knockdown cells (Figs. 2F, G and S8H). To evaluate the potential off-target effects of the TDF sensor in recognizing other circRNAs, we employed CRISPR-Cas9 technology to generate a *Scmh1*-knockout cell line. Using the TDF sensor to detect fluorescence signals, we observed that the fluorescence nearly disappeared following the knockout of all *Scmh1*-related linear and circular transcripts compared to the vector group (Fig. S9A–C). These results demonstrate the high specificity of the TDF sensor for binding of circSCMH1, but not linear *Scmh1* mRNA.

To assess whether the binding of the TDF sensor affects the function of circSCMH1, we analyzed whether the TDF sensor impacts the interaction between circSCMH1 and methyl-CpG-binding protein 2 (MeCP2) or fat mass and obesity associated protein (FTO)^{20,21} since the circSCMH1 exerted biological function via binding with these RNA-binding proteins. At the binding site level, circSCMH1 binds to MeCP2 and FTO at positions 426–485 and 426–477, respectively, without

overlap with the binding site of TDF sensor (Fig. S10A). To further rule out any potential effect of the TDF sensor on circSCMH1's spatial conformation and function, RIP experiments were performed and showed that the addition of the TDF sensor did not affect the binding of circSCMH1 to MeCP2 and FTO (Fig. S10B). This indicates that the TDF sensor does not impact the function of circSCMH1. Additionally, to evaluate the potential interference of RBPs on the binding between the TDF sensor and circSCMH1, circSCMH1 was detected in HT-22 cells using the TDF sensors. It was observed that the overexpression of MeCP2 did not significantly affect the TDF sensor's recognition signal for circSCMH1, as detected by confocal laser scanning microscopy (Fig. S10C, D).

Dynamic real-time monitoring of circSCMH1 in cultured neurons

Encouraged by fast speed and high sensitivity of TDF sensor, and taking advantage of high membrane permeability and high biostability of the TDF sensor, it was then used to visualize circSCMH1 in cultured cells. HT-22 cells were incubated with TDF sensor to investigate the efficiency of circSCMH1 recognition at various time points. Firstly, CCK8 assay indicated that TDF sensor did not affect the cell viability (Fig. 3A), revealing good biocompatibility of TDF sensor. Then, using a live cell imaging system, we dynamically and in real-time monitored circSCMH1 in HT-22 cells using the TDF sensor (Fig. 3B). Fluorescence signal was observed in living HT-22 cells upon incubation with TDF sensor from 3 to 12 h, and the fluorescence signal increased in a time-dependent manner (Fig. 3B–D and Movie S1). Moreover, we performed

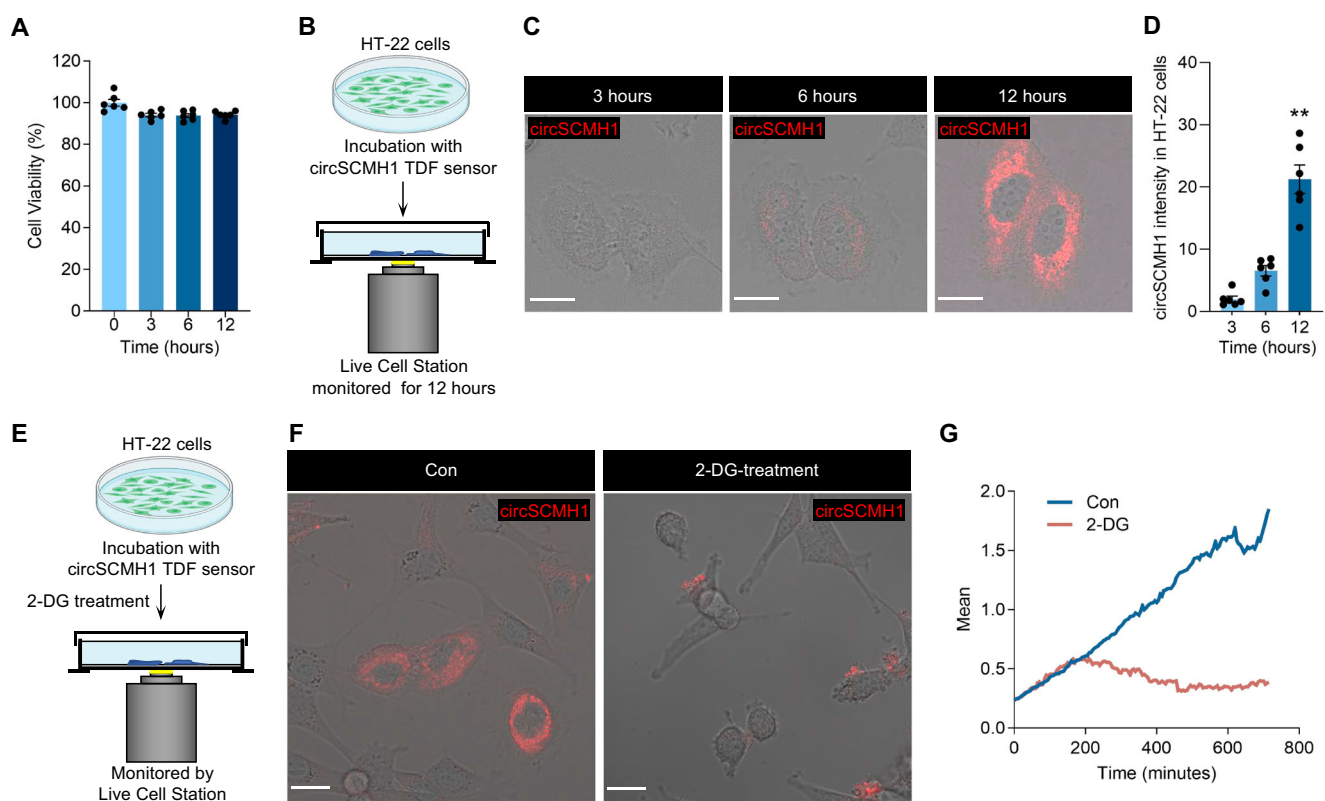


Fig. 3 | Using TDF sensor to image circSCMH1 in cultured neurons. **A** CCK8 assay was used to detect the cell viability of HT-22 cells under TDF sensor incubation for 0, 3, 6, and 12 h. Data are presented as mean \pm SEM, $n = 6$ biological replicates/group. **B** Schematic diagram of the approach for monitoring circSCMH1 in HT-22 cells using a live cell station. Created in BioRender. Yao, H. (2024) BioRender.com/v74m668. **C** Images of circSCMH1 in HT-22 cells after incubation with TDF sensor for 3, 6, and 12 h. Red, circSCMH1. Scale bar, 20 μ m. **D** Quantification of circSCMH1 intensity in HT-22 cells. Data are presented as mean \pm SEM, $n = 6$ images (selected 5 representative cells in each image for quantification)/group. $^{*}P = 0.0016$ versus 3 h

using one-way Friedman test followed by the Dunn's multiple comparisons test. **E** Schematic diagram of the approach for monitoring circSCMH1 in HT-22 cells after 2-DG treatment using a live cell system. Created in BioRender. Yao, H. (2024) BioRender.com/v74m668. **F** Images of circSCMH1 in HT-22 cells after treatment with 2-DG and incubation with TDF sensor for 12 h. Red, circSCMH1. This experiment was repeated at least three independent experiments. Scale bar, 20 μ m. **G** Quantification of circSCMH1 intensity in HT-22 cells under control and 2-DG treatment condition. Con, control; 2-DG, 2-Deoxy-D-glucose. Source data are provided as a Source Data file.

real-time monitoring of the fluorescence signal in HT-22 cells treated with the TDF sensor for a duration of 24 h. During this time, the fluorescence signal reached a plateau at approximately 13.7 h after incubation and started to decrease around 16.3 h. In contrast, the *Scmhl1*-knockout cell line, used as a control, exhibited no fluorescence signal (Fig. S11A, B). The dynamic imaging of circSCMH1 in living cells achieved by TDF sensor represents a groundbreaking advancement in the field of circRNA detection, which are essential for the deep understanding of the underlying circRNA dynamics and functions.

Previous results demonstrated that ischemia results in the significant reduction in circSCMH1 expression²⁰. Thus, we further explored its application to monitor the intracellular expression of circSCMH1 under oxygen-glucose deprivation (OGD) condition. To address this issue, HT-22 cells were subsequently co-incubated with the 2-deoxy-Glucose (2-DG, chemical compound mimics the condition of OGD) and the TDF sensor (Fig. 3E). The dynamic response of HT-22 to 2-DG treatment was observed using a live cell imaging system, characterized by discernible reduction in fluorescence signal compared to control condition, indicating that circSCMH1 was reduced after OGD treatment (Fig. 3F, G, Movie S2). Additionally, imaging of HT-22 cells under OGD condition using the TDF sensor further confirmed the phenomenon of reduced circSCMH1 levels after OGD treatment (Fig. S12A–C). Taken together, these results demonstrate that the TDF sensor is suitable for the detection of circRNAs in living cells, providing a sensitive, specific, and stable fluorescence in response to circSCMH1.

Previous studies reported that the TDF nanostructure were able to cross cell membrane via caveolae-mediated endocytosis^{22,23}. Thus, to investigate the endocytosis mechanism of TDF sensor, the transcellular transport of TDF into HT-22 cells treated with the endocytosis inhibitors, chlorpromazine (for clathrin-mediated endocytosis) or genistein (caveolae-mediated endocytosis) was monitored by confocal fluorescence imaging. As shown in Fig. S13A, B, pretreatment of HT-22 cells with genistein exhibited a significant decrease of the cellular uptake efficiency, while pretreatment with chlorpromazine did not reduce the uptake of TDF sensor. These results demonstrate that TDFs are internalized through the caveolae-mediated endocytosis pathway.

Next, we sought to examine the structural integrity of TDF sensors upon being taken up by living cells. Cy3 dye and Cy5 dye as a Förster resonance energy transfer (FRET) pair were labeled on the same vertex of TDF sensor nanostructures followed by the incubation with HT-22 cells for 24 h. As shown in Fig. S14, fluorescence emission signals of Cy3 (green color) and FRET (red color) on TDFs were observed and the merged image showed the yellow overlapping signal of Cy3 and FRET in the system, suggesting TDF sensor taken up by the live cells still remained as intact structures, which is consistent with the previous studies²⁴. To further explore the stability of TDF sensor in mice blood serum, the TDF sensors were incubated with mice blood serum for a period time. As shown in Fig. S15, the strips of TDF nanostructures were clearly observed until 24 h, which indicated that the TDF nanostructures could remain stable in the bloodstream. The results suggest that TDF sensor are reliable and feasible to use for in vitro and in vivo research.

Dynamic real-time monitoring of circSCMH1 in freely moving mice

Detecting and tracking the dynamic changes of circRNAs in vivo is crucial for exploring the functional significance of circRNAs, and the relevant technology remains largely undeveloped. In order to verify in vivo delivery of TDFs, the biodistribution was investigated in mice. Cy5-labelled TDFs were delivered by tail-vein injection, and in vivo fluorescence images after injecting TDF sensors were recorded at different time points (10, 20, 30, 40, 50, and 60 min). As shown in Fig. S16A, fluorescent signals were detected in the different organs including heart, liver, spleen, lung, kidney, and brain. Notably, an

evident fluorescent signal was also detected in brain of the mice, indicating that TDFs was able to cross the blood-brain barrier and accumulate in the brain after systematic injection. Ex vivo fluorescence images of major organs (e.g., heart, liver, spleen, lung, kidney, and brain) also correspond well with the biodistribution data (Fig. S16B, C).

Subsequently, we affixed a triangular headpiece to the cranial window to establish a specific surgical field. This step ensured the free movement of mice while facilitating the connection of the imaging device. Following the induction of stroke in mice at day 14, the TDF sensor was administered via tail vein injection. In vivo dynamic imaging of circSCMH1 was subsequently accomplished using a fast, high-resolution, miniaturized two-photon microscope²⁵. This advanced imaging technique facilitated real-time monitoring of circSCMH1 levels at depths of up to 600 μm in the brain, and the observations were conducted through a chronically implanted cranial window (Fig. S17A). We found that a stable fluorescence signal was present between 3 to 12 h after tail vein injection of the two-photon dye-functionalized TDF sensor (Fig. S17B, C). Therefore, in subsequent experiments, we performed tail vein injections of the TDF sensor for 6 h before detection, focusing specifically on the distribution of circSCMH1 in the L2/3 layer of the cerebral cortex. The workflow for detecting the changes in circSCMH1 after stroke using the TDF sensor is illustrated in Fig. 4A. By tracking for 7 days under the two-photon microscopy, we found the significant decrease in the real-time abundance of circSCMH1 in the peri-infarct area with the prolonged duration after stroke (Fig. 4B, C), which was further confirmed by qPCR analysis (Fig. S18). The real-time, in vivo tracking of circSCMH1 in the cerebral cortex of freely moving animals represents a significant breakthrough in the field of circRNA imaging enabled by the TDF sensor.

Sensitive and fast in situ imaging of circSCMH1 in mouse brain sections

However, what are the advantages of using the TDF sensor compared to traditional probe-based in situ hybridization techniques? Therefore, we determined whether the TDF sensor could be utilized for the detection of endogenous circSCMH1 in a physiologically relevant system, specifically in acute mouse brain slices. We performed specific labeling of neurons and astrocytes in mouse brain slices while employing the TDF sensors for in situ imaging of circSCMH1 (Fig. 5A). Colocalization with the neuron-specific marker NeuN unveiled a high abundance of circSCMH1 expression in neurons (Fig. 5B). As the incubation time of brain slices with TDF sensors increased, the fluorescence signal intensity at 12 h reached 3.48 times that at 3 h (Fig. 5C). In addition, we also investigated the impact of different temperatures on the TDF sensor's recognition of circSCMH1 in neurons, revealing that 37 °C favored the binding between the TDF sensor and circSCMH1 (Fig. S19A, B). Subsequently, the TDF sensors was applied to detect circSCMH1 in astrocytes, another abundant cell type in the brain, by co-labeling with astrocyte marker GFAP. The TDF sensors facilitated the characterization of circSCMH1's single-cell distribution patterns in astrocytes (Fig. S20A). Importantly, in line with observations in neurons, the TDF sensors revealed a noteworthy surge in signal values for circSCMH1 following a 12-h co-incubation with brain slices (Fig. S20B). Furthermore, distinct fluorescence signals were observed in neurons, whereas astrocytes exhibited weak fluorescence, suggesting that the expression of circSCMH1 is higher in neurons compared to astrocytes. These results indicate that the expression pattern of circSCMH1 is specific to certain cell types, exhibiting varying levels of abundance across different cellular contexts.

While TDF sensors can effectively label endogenous circSCMH1 in brain slices, the question remains as to whether they can reliably detect changes in circSCMH1 within specific cells in the brain slices. We then investigated the utility of the TDF sensor in visualizing circSCMH1 in photothrombotic (PT) stroke model to further expand its application for monitoring circSCMH1 dynamics in vivo. The frozen sections of

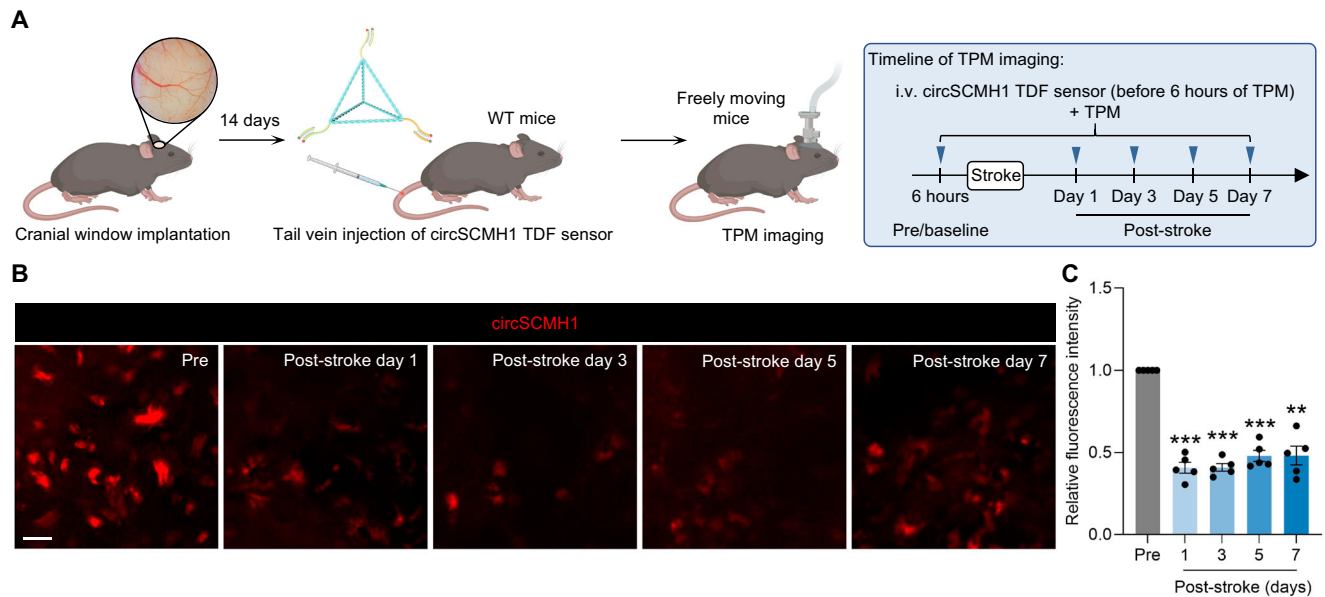


Fig. 4 | Monitoring circSCMH1 in cerebral cortex of freely moving stroked mice.

A Schematic diagram of the experimental design for monitoring circSCMH1 in cerebral cortex using miniaturized two-photon microscope. Mice were injected via tail vein with the TDF sensor at a concentration of 1 μ M, with a volume of 100 μ L per subject. Created in BioRender. Yao, H. (2024) BioRender.com/p66e150.

B Representative images and quantification of circSCMH1 expression in cerebral cortex using miniaturized two-photon microscope from Pre-stroke and Post-stroke

mice. Red, circSCMH1. Scale bar, 20 μ m. **C** Quantitation of fluorescence intensities at different time point before and after stroke. $n = 5$ mice/group. Data are presented as mean \pm SEM, *** $P = 0.0002$ (1 day), *** $P < 0.001$ (3 days), *** $P = 0.0003$ (5 days), and ** $P = 0.0023$ (7 days) versus the Pre group using one-way repeated measures ANOVA followed by Holm–Sidak post hoc multiple comparison test. WT wild type, Pre pre-stroke, TPM two-photon microscopy. Source data are provided as a Source Data file.

mouse brains were conducted on day 3 post-stroke and circSCMH1 was co-labeled with NeuN and GFAP (Fig. 5D). The level of circSCMH1 was significantly reduced in neurons after stroke detected by the TDF, as evidenced by significant decrease of fluorescence signals (Fig. 5E, F). In addition, similar to our results obtained in neurons, we observed significant decrease of the fluorescence signal detected by TDF sensor recognizing circSCMH1 in astrocytes after stroke (Fig. S20C, D). These results demonstrated that the TDF accurately perceived changes in circSCMH1 expression in tissues.

We further compared the performance of the TDF sensor with the conventional probe, which was designed based on the BSJ of circSCMH1. Firstly, we compared the experimental procedures by using previous reported probe and TDF sensor, respectively. As shown in Fig. 5G, traditional in situ hybridization immunofluorescence imaging experiments based on the reported probes require 39 h and involve the cumbersome steps of preparing the hybridization buffer. However, employing TDF sensors reduces the experimental time to 12.75 h, substantially streamlines complex operational procedures, eliminates the need for specific temperature environment control, thereby minimizing interference factors on the experimental results (Fig. 5H).

Additionally, comparison of the imaging results indicated that the traditional in situ hybridization probe exhibited low fluorescence in both neurons and astrocytes, with a brightness 5-fold weaker than that of the TDF sensor (Figs. 5I, J and S20E, F). Collectively, these results suggest that the TDF sensor is well-suited for application in various cell types of tissue sections, exhibiting a sensitive and stable fluorescence increase in response to endogenous circRNA through a rapid and economy manner.

Ultrafast circRNA detecting in unamplified RNAs from clinical samples

The assessment of clinical samples introduces increased biological complexity, coupled with uncertainties arising from inter-patient variations and the procedures employed in sample collection and

preparation²⁶. Furthermore, circRNAs generally exhibit lower expression levels compared to linear RNAs²⁷. Therefore, ultrasensitive and ultrafast detection of circRNAs in clinical samples is crucial for its future application in diagnosing disease and evaluating the efficacy of treatments. To evaluate the feasibility of TDF sensor on circRNA detection from clinical samples, we extracted total RNAs from plasma of 29 healthy controls and 29 AIS patients, respectively. The demographic and clinical characteristics of discovery samples were presented in Table S2. Subsequently, the RNA samples were co-incubated with TDF sensor and the results were measured using a fluorescence detector (Fig. 6A). Without nucleic acid amplification, TDF sensor accurately detected circSCMH1 in plasma samples, as evidenced by significantly higher fluorescence signals observed in the healthy controls group compared to the group of AIS patients (Fig. 6B). We simultaneously reverse transcribed of total RNAs from the same batch of clinical samples and further conducted circSCMH1 detection through qPCR. Consistent with our previous findings, circSCMH1 was significant decreased in the plasma of AIS patients (Fig. 6C). Additionally, the signals in TDF sensor exhibited a positive correlation with the results of qPCR (Fig. 6D). Nonetheless, unlike qPCR, the TDF sensor eliminates the need for an additional target amplification step that requires multiple enzymes and procedures, hence exhibiting the advantages in simplicity, easy operation, and versatility. Together, these results demonstrate that TDF sensor is capable to directly detect circRNAs in clinical samples with ultrafast response as well as excellent sensitivity and accuracy.

Tracking exogenous circSCMH1 in vivo

While the TDF sensor demonstrated high sensitivity and efficacy in detecting endogenous circSCMH1 in both in vitro and in vivo systems, the inability to trace exogenous circSCMH1 delivered to the brain in vivo has been an unresolved challenge during our investigation of its therapeutic efficacy. Therefore, we incubated the TDF sensor with extracellular vesicles (EVs) encapsulating circSCMH1 in vitro, simultaneously utilizing Dio or Dil to label the EV membranes. A triangular

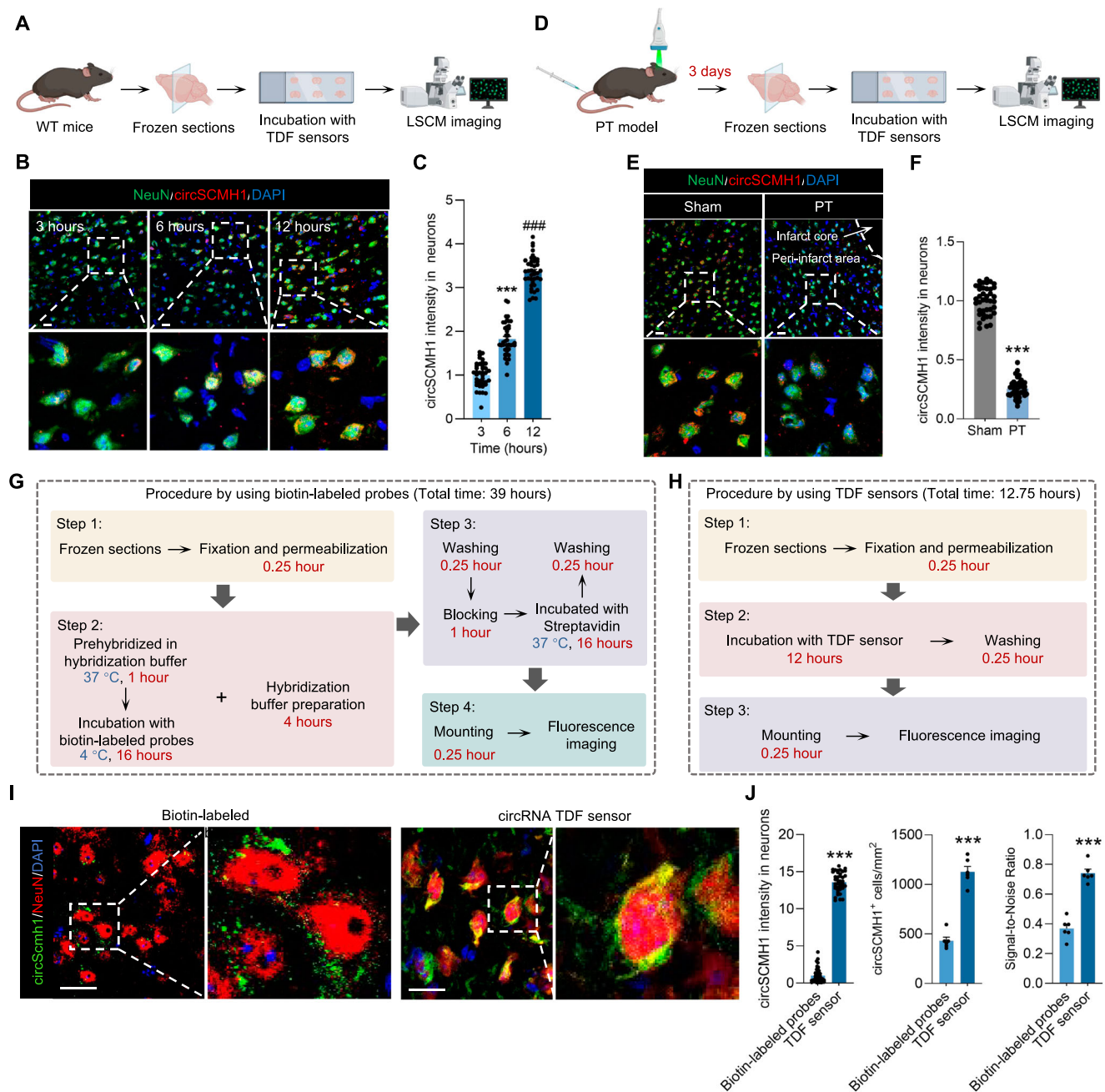


Fig. 5 | In situ imaging of circSCMH1 in mouse brain sections. **A** Schematic diagram of the experimental design for in situ imaging circSCMH1 in mouse brain sections. Created in BioRender. Yao, H. (2024) BioRender.com/w93y687. **B** Colocalization of NeuN and circSCMH1 in mouse brain sections after incubation with TDF sensor for 3, 6, and 12 h. Green, NeuN; Red, circSCMH1; Blue, DAPI. Scale bar, 20 μ m. **C** Quantification of circSCMH1 intensity in neurons. Data are presented as mean \pm SEM, $n = 4$ slices (selected 10 representative cells in each slice for quantification) from 4 mice/group. *** $P < 0.001$ versus 3 h, ### $P < 0.001$ versus 6 h using one-way ANOVA followed by Holm–Sidak post hoc multiple comparison test. **D** Schematic diagram of the experimental design for in situ imaging circSCMH1 in PT mouse brain sections. Created in BioRender. Yao, H. (2024) BioRender.com/w93y687. **E** Colocalization of NeuN and circSCMH1 in brain sections of Sham and PT mice after incubation with TDF sensor for 12 h. Green, NeuN; Red, circSCMH1; Blue, DAPI. Scale bar, 20 μ m. **F** Quantification of circSCMH1 intensity in neurons. Data are

presented as mean \pm SEM, $n = 4$ slices (selected 10 representative cells in each slice for quantification) from 4 mice/group. *** $P < 0.001$ versus Sham group using unpaired two-tailed Student's t test. **G** The procedure of in situ imaging using biotin-labeled probes. **H** The procedure of in situ imaging using TDF sensors. **I** Representative images of the colocalization of NeuN and circSCMH1 in mouse brain sections using biotin-labeled probes and TDF sensors respectively. Green, circSCMH1; Red, NeuN; Blue, DAPI. Scale bar, 20 μ m. **J** The plots were the analysis of circSCMH1 intensity, circSCMH1⁺ cells/mm², and signal-to-noise ratio in neurons. Data are presented as mean \pm SEM, $n = 4$ slices (selected 10 representative cells in each slice for quantification) from 4 mice/group for the analysis circSCMH1 intensity, circSCMH1⁺ cells/mm², and signal-to-noise ratio. *** $P < 0.001$ versus biotin-labeled probes using unpaired two-tailed Student's t test. WT wild type, PT photothrombotic, LSCM laser scanning confocal microscope. Source data are provided as a Source Data file.

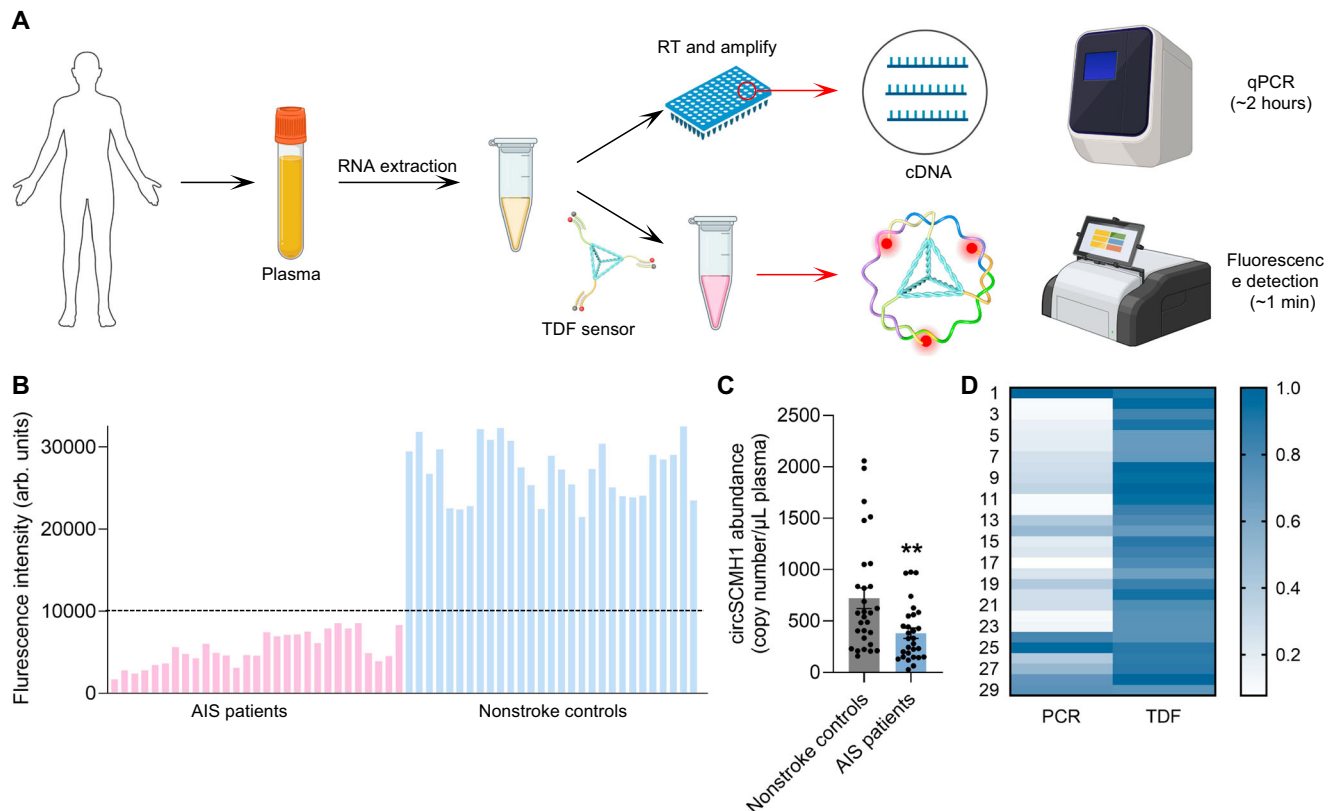


Fig. 6 | Detecting circRNA in unamplified RNAs from clinical samples.

A Schematic diagram of the experimental design for detecting circSCMH1 in total RNAs from clinical samples. Created in BioRender. Yao, H. (2024) BioRender.com/c36h692. **B** Quantification of circSCMH1 fluorescence intensity in unamplified RNAs from the plasma of nonstroke controls and AIS patients. $n = 29$ samples/group. **C** qPCR analysis of circSCMH1 in total RNAs from nonstroke controls and AIS

patients. Data are presented as mean \pm SEM, $n = 29$ samples/group. $^*P = 0.0039$ versus nonstroke controls using two-tailed Mann–Whitney U test. **D** Heatmap of the normalized signal intensities of 29 AIS patient samples in TDF and qPCR. AIS acute ischemic stroke, RT reverse transcription, arb. units arbitrary units. Source data are provided as a Source Data file.

headpiece was affixed to the cranial window to establish a specific surgical field. On the third day post-modeling, the EVs were administered via tail vein or intranasal injection, and two-photon imaging was conducted at 4 h after the injection. The results provide clear visualization of the in vivo tracking of green-colored Dio⁺ EVs and red-colored circSCMH1, enhancing the accuracy and reliability of our observations (Fig. 7A–D).

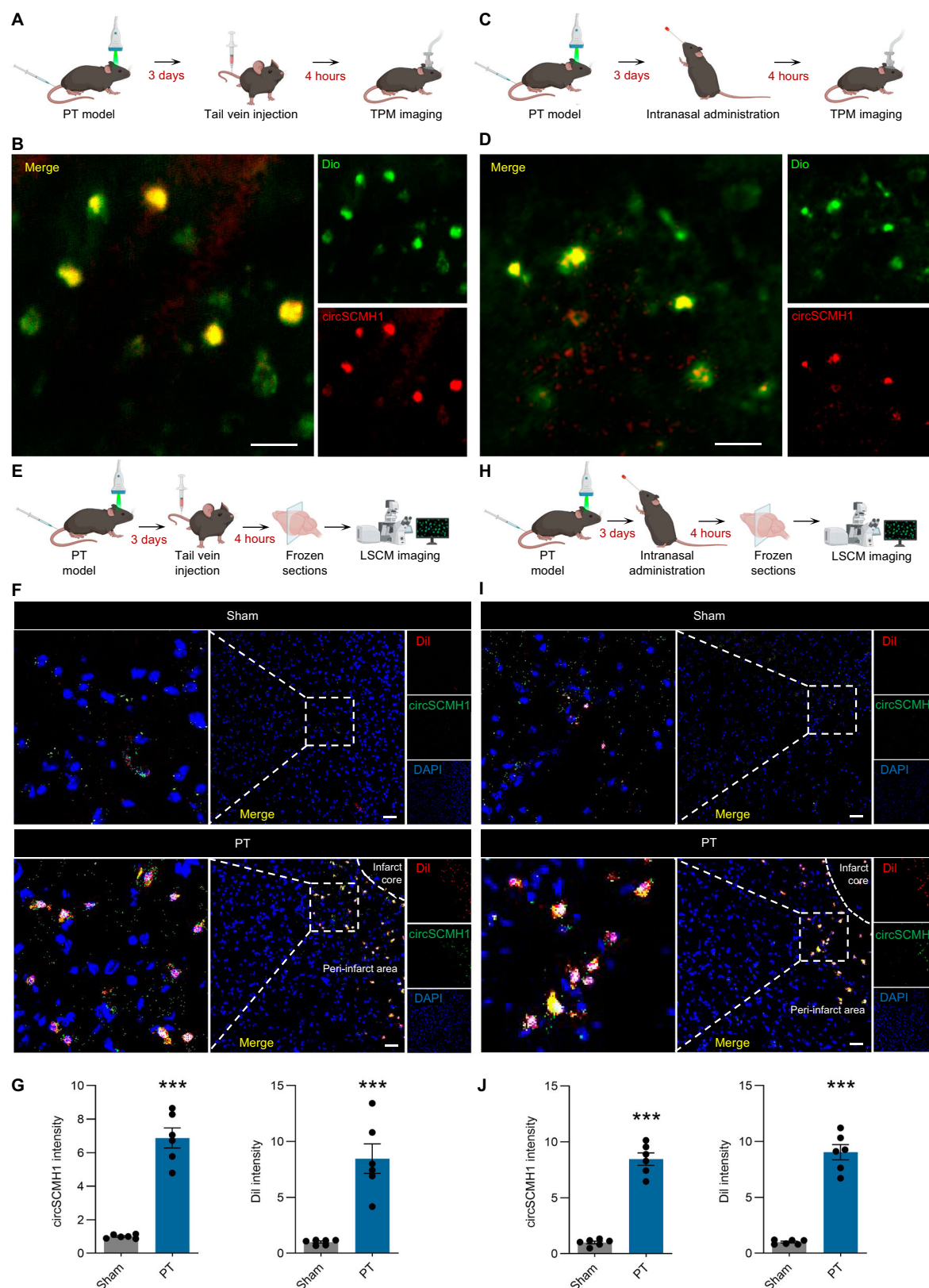
Then, we obtained brain frozen sections from both sham and PT mice, followed by imaging circSCMH1-EVs using microscope (Fig. 7E). The red-colored Dio⁺ EVs were enriched in the peri-infarct area of PT mouse brains, which co-localized with the green-colored circSCMH1 detected by TDF sensor (Fig. 7F, G). In contrast, these elements showed a diffuse distribution in the brains of sham mice (Fig. S21). Since nasal administration of EVs is considered one of the most promising routes for clinical application, we next traced exogenous circSCMH1 in vivo and observed that the co-localization of red-colored Dio⁺ EVs and green-colored circSCMH1 detected by TDF sensor (Fig. 7H–J). These results indicate that the TDF sensor can effectively trace exogenous circRNA in vivo, addressing the pharmacological evaluation challenges that hinder the development of nucleic acid drug based on circRNAs.

Discussion

In the current study, we report the development and characterization of a sensitive and fast sensor called TDF sensor for the selective recognition and high-affinity capture of intact circRNAs. The TDF sensor engages with circRNAs through pattern-matching and multi-valent interactions, thereby enabling the efficient capture of circRNAs.

Consequently, TDF sensor can be used to visualize the real-time response of endogenous circRNA in vitro cultured neuronal cells and in vivo brain with miniaturized two-photon microscopy. Moreover, the TDF sensor enables high sensitivity and fast detection of circRNA expression in brain tissue and clinic samples compared with the traditional in situ hybridization and qPCR, respectively. In addition to the detection of endogenous circRNA, the TDF sensor was expanded to reveal the distribution of exogenous circRNA delivered into the brain by EVs.

The TDF sensor has at least five distinct advantages over other methodologies with respect to detection of circRNA: (1) TDF sensor exhibited fast recognition for the circRNA, as that only 1 min was needed to detect the circRNA in our study with sharp contrast to other diagnostic analytic technologies^{6,7,28} such as qPCR (120 min), netlike hybridization chain reaction (180 min), and CRISPR assay (210 min); (2) TDF sensor was characterized by higher sensitivity for specific recognition of circRNA due to the precise spatial pattern-recognition properties compared with the previous methods, thus enabling for the ultraprecise detection of unamplified circRNAs in different samples; (3) TDF sensor offered easy-operation of circRNA detection compared with the previous methods involving laborious processes, trained personnel, and specialized tools, thus avoiding the biased results due to the complicated operation; (4) TDF sensor allowed for the visualization for the real-time response of endogenous circRNA in vitro cultured cells and in vivo brain with miniaturized two-photon microscopy. Particularly, upon direct addition of TDF to the culture medium or injection of TDF sensor into the mouse, live-cell imaging of endogenous circRNAs was achieved, while other methods cannot



provide so far; (5) TDF sensor allowed for tracing of the exogenous circRNAs after incubation with circRNA in vitro and subsequent injection of the TDF sensor-circRNAs into the body, accomplishing in vivo tracing of exogenous circRNAs, which resolved the bottleneck issues in tracking the in vivo behavior of nucleic acid drugs developed based on circRNAs. To our knowledge, tracing the distribution of exogenous circRNAs has not been reported.

The expression of circRNA exhibits highly conditional and spatiotemporal specificity^{3,29}. After validating the performance of the TDF sensor in cells, we applied it to investigate the real-time response of circRNA in different conditions. We revealed that OGD treatment induced the decreased level of circSCMH1, consistent with our previous results²⁰. We further investigated circSCMH1 abundance in freely moving PT-stroked mice and dynamically observed that the level of

Fig. 7 | Tracking EV-delivered exogenous circSCMH1 in vivo. **A** Schematic diagram of the experimental design for tracking EV-delivered exogenous circSCMH1 in mice after tail vein injection of EVs using TPM. Created in BioRender. Yao, H. (2024) BioRender.com/m46e219. **B** Representative images of EV-delivered exogenous circSCMH1 in cerebral cortex using TPM from post-stroke mice. Green, Dio; Red, circSCMH1. $n = 3$ mice/group. Scale bar, 20 μm . **C** Schematic diagram of the experimental design for tracking EV-delivered exogenous circSCMH1 in mice after nasally administering of EVs using TPM. Created in BioRender. Yao, H. (2024) BioRender.com/m46e219. **D** Representative images of EV-delivered exogenous circSCMH1 in cerebral cortex using TPM from post-stroke mice. Green, Dio; Red, circSCMH1. $n = 3$ mice/group. Scale bar, 20 μm . **E** Schematic diagram of the experimental design for tracking EV-delivered exogenous circSCMH1 in mice after tail vein injection of EVs using LSCM. Created in BioRender. Yao, H. (2024) BioRender.com/m46e219. **F** Co-localization of Dil and circSCMH1 in brain sections of

Sham and PT mice after tail vein injection of EVs for 4 h. Green, circSCMH1; Red, Dil; Blue, DAPI. Scale bar, 40 μm . **G** Quantification of circSCMH1 and Dil intensity in brain slices. Data are presented as mean \pm SEM, $n = 6$ mice/group. $^{***}P < 0.001$ versus Sham group using unpaired two-tailed Student's t test. **H** Schematic diagram of the experimental design for tracking EV-delivered exogenous circSCMH1 in mice after nasally administering of EVs using LSCM. Created in BioRender. Yao, H. (2024) BioRender.com/m46e219. **I** Co-localization of Dil and circSCMH1 in brain sections of Sham and PT mice after nasally administering of EVs for 4 h. Green, circSCMH1; Red, Dil; Blue, DAPI. Scale bar, 40 μm . **J** Quantification of circSCMH1 and Dil intensity in brain slices. Data are presented as mean \pm SEM, $n = 6$ mice/group. $^{***}P < 0.001$ versus Sham group using unpaired two-tailed Student's t test. PT photothrombotic, LSCM laser scanning confocal microscope. Source data are provided as a Source Data file.

circSCMH1 decreased in the context of stroke, indicating an inverse association between circSCMH1 abundance and ischemic injury. Furthermore, the TDF sensor, compared to traditional probes, is well-suited for tissue sections, displaying a rapid, cost-effective, and stable fluorescence increase in response to endogenous circRNAs. This advantage enables us to achieve precise subcellular localization of circRNAs. In order to further expand the clinical applications of the TDF sensor, we utilized it to evaluate the circRNA abundance in clinical samples from AIS patients, demonstrating its ultrafast circRNA detection capability. At the end, the TDF sensor was applied to track the distribution of exogenous circRNAs in vivo, highlighting its potential to enhance the investigation of nucleic acid drugs.

Taken together, our study demonstrates the versatile application of the TDF sensor for rapid detection of circSCMH1 both in vitro and in vivo. (i) Given the high cellular uptake efficiency of TDF sensor, the imaging of subcellular location-specific expression of circSCMH1 may be envisaged, which will enrich our understanding of the mechanisms and functions of circSCMH1 at the subcellular levels. (ii) TDF sensors have been successfully used for detection and imaging of circSCMH1 with high sensitivity and precision. However, considering tens of thousands of circRNA existed in the cells, our strategy can be extended to detect other disease-associated circRNAs by designing DNA nanoarchitectures. (iii) TDF developed here fulfill the requirements for rapid detection and imaging of single circRNA in mammalian cells. In the future, it would be possible to develop TDF sensors for multiplexed circRNA imaging to explore the functionality and mechanism of multiple circRNAs underlying diverse biological processes. (iv) Further development of portable systems allows for point-of-care testing of circRNAs in clinics and at home.

The TDF sensor-based detection technology for circRNA also has some limitations. Given the necessity of BSJ for the specific detection of circRNA and the potential risks of RBP binding to BSJ, whether the RBP binding to BSJ sequence affects the design of other TDF sensors should be investigated. Thus, additional experiments should be undertaken in the future work, for example, protease treatment of fixed cells before probe hybridization⁷. In addition, a limitation of the present study is its reliance on software such as RNAfold for predicting circRNA structures. Future efforts might develop RNA structure analysis techniques to determine circRNA structures, so as to increase the accuracy of circRNA structure, thereby optimizing TDF sensor design.

Methods

Ethical statement

All methods and study materials are available in the article and its Data Supplement or from the corresponding author. All mouse experiments were approved by the Institutional Animal Care and Use Committee at the Medical School of Southeast University, Nanjing, Jiangsu, China (approval ID 20230224036). AIS patients and nonstroke controls were recruited from Jiangsu Province Hospital, Nanjing, Jiangsu, China. This

study was approved by the ethics committees at Jiangsu Province Hospital (approval ID 2020-SR-276).

Human plasma collection

All participants or their legally authorized representatives providing written informed consent prior to participation. Plasma samples were sourced from patients who had not undergone drug therapy within 72 h following the onset of stroke. Upon admission, 5 mL of peripheral blood was collected into EDTA-K2 anticoagulant tubes (BD Biosciences). The samples were then centrifuged at $1000 \times g$ for 10 min at 4 °C. The supernatant was carefully transferred into RNase/DNase-free tubes and stored at -80 °C for future use.

Animals. Physiological differences between male and female mice, including hormone production, prompted us to use an exclusively male animal colony to avoid disruptions from female physiological cycles and minimize experimental variability. The adult male C57BL/6J mice, weighing between 24.0 and 26.0 grams and aged 8 to 10 weeks, were purchased from GemPharmatech in Nanjing, China. These mice were then randomly allocated to different experimental groups. The mice were maintained under stable temperature and humidity conditions, following a 12-h light/dark cycle starting at 7:00 AM. The mice had unrestricted access to food and water. In conducting animal experiments, we adhered strictly to the Animal Research: Reporting of In Vivo Experiments (ARRIVE) guidelines, with efforts made to minimize the number of animals utilized. The sample size was determined based on empirical data from prior studies and aligned with standard practices in the field. Mice were coded and randomly assigned to either experimental or control groups.

Cell culture. The mouse hippocampal neuron HT-22 cells and HEK293T cells were obtained from the Shanghai Cell Bank of the Chinese Academy of Sciences in Shanghai, China. These cells were cultured in DMEM, which was supplemented with 10% fetal bovine serum (FBS) and 1% penicillin-streptomycin. They were maintained in a humidified incubator set at 37 °C with 5% CO_2 .

Preparation and characterization of TDFs. The nucleic acid sequences used in the study were synthesized by Sangon Biotechnology and were purified by high performance liquid chromatography. The nucleic acid sequences of TDFs with different size were provided in Table S1. The nucleic acid strands of different structures were mixed with equimolar ratio in $1 \times \text{PB}$ buffer containing 10 mM $\text{NaH}_2\text{PO}_4/\text{Na}_2\text{HPO}_4$, pH 7.0, and 50 mM MgCl_2 . The mixture was annealed at 95 °C for 10 min and then cooled to 4 °C within 1 min. The successful formation of TDFs with different size was confirmed by agarose gel electrophoresis, and yields of TDFs were semiquantified using ImageJ software. DNA Marker A (25–500 bp), RNase R, and “GelRed nucleic acid gel stain” were obtained from Sangon Biotech. Agarose was purchased from Aladdin Reagent. Ultrapure water (resistance $> 18 \text{ M}\Omega\text{-cm}$)

was used in all of the experiments. The morphology of TDF sensor was demonstrated using the atomic force microscope (AFM). The two-photon fluorophore was synthesized according to the details presented in Fig. S22.

Fluorescence Assay. Fluorescence spectra were recorded with a Fluoromax-4, Horiba Jobin Yvon. For detection of circRNAs, different concentrations of circRNAs were added to 200 μ L of $1 \times$ PB buffer solution containing 100 nM TDF sensor, followed by incubation for 1 min at room temperature. The fluorescence spectra of Cy5 were examined from 640 to 800 nm with excitation wavelength at 620 nm.

Oxygen glucose deprivation (OGD) treatment. HT-22 cells were cultured in a sealed chamber using deoxygenated DMEM without glucose and FBS (11966-025, Gibco), infused with a gas mixture of 5% CO₂ and 95% N₂ at a flow rate of 25 L/min for 5 min (MIC-101, Billups-Rothenburg). The chamber was then placed inside a water-jacketed incubator (Forma, Thermo Fisher Scientific). For the control group, the HT-22 cells were cultured under identical conditions but with standard DMEM and 10% FBS.

2-Deoxy-D-glucose (2-DG) treatment. HT-22 cells were cultured with DMEM containing 5 mM 2-DG (D8375, sigma) for 12 h. The culture conditions were 5% CO₂ and 37 °C. Confocal observation was used at the same time of processing, and signals were collected every five minutes.

CircSCMH1 dynamic imaging. HT-22 cells with a number of 3×10^4 were seeded into a 35 mm confocal dish. The next day, the cultured cells were treated with the circSCMH1 TDF sensor and 2-DG. The dish was then moved to a live-cell imaging workstation, maintained at 37 °C and 5% CO₂. Subsequently, the cells were identified for monitoring, and images were taken every 5 min for a total duration of 12 or 24 h using a confocal microscope (FV3000, Olympus, Japan).

Photothrombotic (PT) stroke mouse model. Focal cortical ischemia was induced in mice via photothrombosis of cortical microvessels, as previously described^{30,31}. In summary, mice were anesthetized using 2% isoflurane (26675-46-7, Keyuanpharm) and secured in a stereotaxic apparatus. Their body temperature was maintained at 37.0 ± 0.5 °C using a homeothermic blanket throughout the procedure. After making a midline skin incision and clearing connective tissues, the skull was exposed and kept dry. An opaque template with a 2 mm diameter and 12,000 lux illumination opening, connected to a cold light source (World Precision Instruments, USA), was positioned 1.5 mm lateral to the bregma. Five minutes following the intravenous administration of Rose Bengal (30 mg/kg, 330,000, Sigma), the brain was exposed to light for 5 min. This light exposure prompted the generation of singlet oxygen from Rose Bengal, damaging and occluding the vascular endothelium, and thus causing a focal cortical stroke. Sham-operated mice were administered the same Rose Bengal dose but did not undergo illumination.

Cranial window implantation. About two weeks after the virus injection, the craniotomy surgery was performed on the mice. The anesthetized mice were fixed and a circular cranial window (4.8 mm in diameter) was centered over the targeted cortex. To remove bone pieces, the cranial window surface was cleaned with warm saline. A sterile 4.5 mm circular glass coverslip (0.1 mm in thickness) was implanted into the craniotomy site carefully, and sealed with Tissue adhesive (No1469SB, 3 M). Then the coverslip and headplate were secured over the cranial window with dental cement. The mice were given a recovery period of at least two weeks and were acclimated to head fixation.

Two-photon imaging in awake animals. After two weeks of fixing the headplate, the mouse was restrained with a body holder, then the benchtop two-photon microscope was used to find the region of viral infection.

The fast, high-resolution, miniaturized two-photon microscope (FHIRM-TPM) with a femtosecond fiber laser (~35 mW at the objective, TVS-FL-01, Transcend Vivoscope Biotech Co., Ltd) was employed for two-photon imaging³². Once the field of view was found with FHIRM-TPM, the holder was glued to the headplate permanently and the objective was connected to the holder with three screws. The gap between the objective and the coverslip was filled with 1.5% low-melting-point agarose. The GINKGO-MTPM software (GINKGO-MTPM 1.0.28, Transcend Vivoscope Biotech Co., Ltd) was used for microscope control and image acquisition. All images were acquired at a frame of 10 Hz (512×512 pixel) and field of view was $420 \mu\text{m} \times 420 \mu\text{m}$. After imaging, the objective was dismounted by unscrewing and unplugging from the holder.

Quantitative polymerase chain reaction (qPCR). RNA was extracted with TRIzol reagent (9109, Takara) following the manufacturer's protocol. Reverse transcription was conducted with the HiScript Q RT SuperMix for qPCR Kit (R123-01, Vazyme), and quantification was achieved using SYBR Green qPCR Master Mix (Q141-02, Vazyme), adhering to the manufacturer's instructions on an Applied Biosystems qPCR System (StepOne, Thermo Fisher, USA). GAPDH served as the internal control. The primers were produced by Invitrogen, with their sequences detailed in Table S1.

To estimate the copy number of circSCMH1 in AIS patient plasma, a specific 402 bp segment encompassing the back-spliced junction of circSCMH1 was cloned into the pUC57 vector (Genscript, Nanjing). The plasmid was then serially diluted by factors of ten to generate a standard curve via real-time PCR. The formula applied to determine the standard's copy number was: copy number (copies/ μL) = $6.02 \times 10^{23} \times \text{plasmid concentration (ng}/\mu\text{L}) \times 10^{-9} / [(\text{molecular weight of vector} + \text{molecular weight of inserted fragment}) \times 660]$ (g/mol). The standard curve yielded a linear relationship described by the equation $Y = aX + b$, where the x -axis (X) represented the log base 10 of the initial copy number and the y -axis (Y) represented the cycle number. The cycle threshold (C_t) values of circSCMH1 were then used with this equation to determine the copy numbers present in the samples.

Immunofluorescence staining and confocal imaging. To study the cellular localization of RVG-EVs in the mouse brain, EVs were labeled with Dil (C1036, Beyotime) and then administered intravenously. After six hours, the mice underwent perfusion with 100 mL PBS followed by 25 mL of 4% PFA. The brains were then extracted and sectioned into slices 30 μm thick. The sections were permeabilized with 0.3% Triton X-100 (T109027, Aladdin) for 15 min and blocked in a solution of 10% normal goat serum (NGS, ZLI-9056, ZSGB-BIO) in 0.3% Triton X-100 for 1 h at room temperature. Immunostaining was performed overnight at 4 °C using either anti-NeuN (1:200, ab177487, Abcam) or anti-GFAP (1:200, G3893, Sigma-Aldrich) antibodies. Post-staining, the sections were washed three times with PBS and incubated for 1 h with Alexa 488-conjugated goat anti-mouse IgG (1:250, A11001, Invitrogen) or anti-rabbit IgG (1:250, A32731, Invitrogen). After a further three PBS washes, the sections were mounted on glass slides, and images were acquired using confocal microscopy (FV3000, Olympus, Japan).

Fluorescence in situ hybridization (FISH). HT-22 cells and brain sections on coverslips were first permeabilized using 0.25% Triton X-100 for 15 min at room temperature. This was followed by an overnight hybridization at 37 °C with 500 nM of a biotinylated circSCMH1 probe. The next day, the coverslips underwent five washes before being blocked in a solution containing 1% BSA

(BS043D, Biosharp) and 3% NGS for 1 h at room temperature. Subsequently, the cells were incubated with streptavidin-FITC (1:250, 434311, Life Technology) in PBS as a secondary antibody overnight at 4 °C. After completing in situ hybridization, coverslips were blocked with a mixture of 1% BSA and 1% Triton X-100 in PBS for 1 h at room temperature. This was followed by incubation with either a rabbit anti-NeuN antibody (1:200, ab177487, Abcam) or a mouse anti-GFAP antibody (1:200, G3893, Sigma-Aldrich) for 24 h. The coverslips were then washed three times in PBS and further incubated with Alexa Fluor 594 goat anti-rabbit IgG (1:250, A-11012, Invitrogen) or goat anti-mouse IgG (1:250, A-11005, Invitrogen). Finally, after three additional PBS washes, the coverslips were mounted onto slides using DAPI solution (0100-20, SouthernBiotech). The sequence of the biotinylated mouse circSCMH1 probe, with biotin at the 5' end, was 5'-aaaTTGGAGGTGTGTAGGACTTTGGTGCCAGGTGG-3'.

Signal to Noise Ratio (SNR). SNR is an index to test the quality of image³³. The SNR of a fluorescence image is the ratio of the fluorescence signal to the background signal. Ten different regions (cells) were selected for each image, the Mean gray value (Mean) and Standard deviation (StdDev) of different regions were obtained by using Image J (1.53k) software. The SNR value of the fluorescence image was obtained according to the following formula.

$$SNR = \frac{Signal_{Mean_AVERAGE} - Background_{Mean_AVERAGE}}{Signal_{StdDev_AVERAGE}}$$

EV staining and exogenous circSCMH1 labeling. RVG-circSCMH1-EVs were initially resuspended in Dulbecco's phosphate-buffered saline (DPBS, Sigma-Aldrich) to reach a protein concentration of 100 µg/mL. The EVs were then labeled with Dil dye by incubating at 37 °C for 15 min. EV-depleted foetal bovine serum (10%) was able to bind with the extra dye. After dilution with DPBS, the EV samples underwent ultracentrifugation at 200,000 × *g* for 2 h at 4 °C followed by gentle resuspension in 2 mL of DPBS. The EVs were then layered onto a 20%–60% discontinuous sucrose gradient and subjected to ultracentrifugation at 10,000 × *g* for 18 h at 4 °C using an XPN-100 ultracentrifuge (Beckman Coulter, USA). Fractions 7–10 were subsequently collected, combined, and diluted to 25 mL with DPBS. Another round of ultracentrifugation at 200,000 × *g* for 2 h at 4 °C was performed to pellet the EVs once more. In the next step, the EV suspension was mixed with Exo-spin™ buffer (EX03-8, Cell Guidance System, England) at a 2:1 ratio. TDF sensors were added, followed by a 5-min incubation. The EVs were transferred to a mini SEC column, centrifuged at 16,000 × *g* for 1 h, and the pellets were resuspended in 100 µL of DPBS.

RNase R treatment. Total RNAs were extracted using TRIZOL lysis. 1 µg of total RNAs were subjected to treatment with 20 units of RNase R (B110087, Sangon Biotech) in a reaction buffer containing 20 mM Tris-HCl (pH 8.0), 100 mM KCl, and 0.1 mM MgCl₂. The treatment was carried out at 37 °C for 30 min. Subsequently, RNase R was inactivated by heating the sample to 70 °C for 10 min. Reverse transcription was then performed using HiScript Q RT SuperMix for qPCR (R123-01, Vazyme).

RNA-binding protein immunoprecipitation (RIP). RIP was conducted using the Magna RIP™ RNA-binding protein immunoprecipitation kit (17–700, Millipore) as per the manufacturer's protocol. In brief, HT-22 cells, either treated with TDF sensors or left untreated for 12 h, were harvested in 0.5 mL of lysis buffer. Magnetic beads were then incubated with 5 µg of either the anti-FTO antibody (MA5-33105, Invitrogen) or the MeCP2 antibody (SAB4800012, Sigma) in RIP washing buffer, with gentle rotation for at least 1 h at room temperature. Subsequently, the RIP lysates were incubated overnight at 4 °C with the beads bound to the antibody in RIP buffer. After discarding the

supernatant, the pellet was the resuspended in immunoprecipitation buffer containing proteinase K followed by the incubation at 55 °C for 30 min to break down the proteins. The extracted RNA was then utilized for assessing circSCMH1 expression using qPCR.

In vivo imaging and biodistribution studies in mice after tail vein injection of TDF sensor. Organ-specific localization of Cy5-labeled TDF sensors. The fluorescence spectra of Cy5 were examined from 640 to 800 nm with excitation wavelength at 620 nm. Mice were administered a 50 µmol/kg dose of the TDF sensor via intravenous injection. Fluorescence intensity and distribution were captured in vivo at various time points (0, 10, 20, 30, 40, 50, and 60 min) using the IVIS Spectrum Imaging System (PerkinElmer, USA). For ex vivo analysis, mice were euthanized at 0, 10, 20, 30, 40, 50, and 60 min post TDF sensor injection through saline perfusion, followed by dissection and fixation of the brain, heart, liver, and kidneys in 4% paraformaldehyde. Fluorescence signals from the TDF sensor were evaluated using Living Image 4.4 software (PerkinElmer, USA).

Chlorpromazine and genistein treatment. HT-22 cells were cultured with 200 µM chlorpromazine and 2 mM genistein for 1 h. Then the inhibitor was washed off and 1 ml of medium mixed with 100 nM TDF sensor was added and incubated for 12 h. Images were captured by confocal microscopy (FV3000, Olympus, Japan).

Statistics & Reproducibility. Statistical analysis was performed using GraphPad Prism 8.0.2 Software (GraphPad Software, USA). Significance was assessed with the two-tailed Student's *t* test for comparisons of 2 groups or Mann–Whitney *U* test for nonnormally distributed data. One-way ANOVA followed by the Holm–Sidak post hoc test were used for multi-group (3 or more) comparisons. Kruskal–Wallis test followed by the Dunn's multiple comparisons test were used for multi-group (3 or more) comparisons of nonnormally distributed data. Data collected at multiple, sequential time points were analyzed using one-way repeated-measures ANOVA followed by the Holm–Sidak post hoc test. Nonnormally distributed data collected at multiple, sequential time points were analyzed using one-way Friedman test followed by the Dunn's multiple comparisons test. All data were presented as mean ± SEM. The specific statistical methods used for each experiment are detailed in the figure legends, with a *P*-value of <0.05 considered significant. No statistical method was used to predetermine sample size. No data were excluded from the analyses. The experiments were randomized. No blinding was implemented during data collection, as none of the procedures were susceptible to investigator bias. Data analysis was conducted by investigators who were blinded to the experimental groups.

Reporting summary

Further information on research design is available in the Nature Portfolio Reporting Summary linked to this article.

Data availability

All data generated in this study are present in the main text or the Supplementary Information. Source data are provided with this paper.

References

1. Zhou, W. Y. et al. Circular RNA: metabolism, functions and interactions with proteins. *Mol. Cancer* **19**, 172 (2020).
2. Wilusz, J. E. A 360 degrees view of circular RNAs: from biogenesis to functions. *Wiley Interdiscip. Rev. RNA* **9**, e1478 (2018).
3. Liu, C.-X. & Chen, L.-L. Circular RNAs: characterization, cellular roles, and applications. *Cell* **185**, 2016–2034 (2022).
4. Kristensen, L. S. et al. The biogenesis, biology and characterization of circular RNAs. *Nat. Rev. Genet.* **20**, 675–691 (2019).

5. Dodbele, S., Mutlu, N. & Wilusz, J. E. Best practices to ensure robust investigation of circular RNAs: pitfalls and tips. *EMBO Rep.* **22**, e52072 (2021).
6. Dong, J. et al. Specific and sensitive detection of CircRNA based on netlike hybridization chain reaction. *Biosens. Bioelectron.* **192**, 113508 (2021).
7. Nielsen, A. F. et al. Best practice standards for circular RNA research. *Nat. Methods* **19**, 1208–1220 (2022).
8. Vromman, M. et al. Large-scale benchmarking of circRNA detection tools reveals large differences in sensitivity but not in precision. *Nat. Methods* **20**, 1159–1169 (2023).
9. Sigl, C. et al. Programmable icosahedral shell system for virus trapping. *Nat. Mater.* **20**, 1281–1289 (2021).
10. Kwon, P. S. et al. Designer DNA architecture offers precise and multivalent spatial pattern-recognition for viral sensing and inhibition. *Nat. Chem.* **12**, 26–35 (2019).
11. Song, Y. et al. Bioinspired engineering of a multivalent aptamer-functionalized nanointerface to enhance the capture and release of circulating tumor cells. *Angew. Chem. Int. Ed.* **58**, 2236–2240 (2019).
12. Ma, Y. et al. Spatial imaging of glycoRNA in single cells with ARPLA. *Nat. Biotechnol.* <https://doi.org/10.1038/s41587-023-01801-z> (2023).
13. Ge, Z., Gu, H., Li, Q. & Fan, C. Concept and development of framework nucleic acids. *J. Am. Chem. Soc.* **140**, 17808–17819 (2018).
14. Yin, F. et al. DNA-framework-based multidimensional molecular classifiers for cancer diagnosis. *Nat. Nanotechnol.* **18**, 677–686 (2023).
15. Wang, J., Li, Z. & Willner, I. Dynamic reconfigurable DNA nanostructures, networks and materials. *Angew. Chem. Int. Ed.* **62**, e202215332 (2023).
16. Du, Y. et al. Membrane-anchored DNA nanojunctions enable closer antigen-presenting cell–T-cell contact in elevated T-cell receptor triggering. *Nat. Nanotechnol.* **18**, 818–827 (2023).
17. Walsh, A. S., Yin, H., Erben, C. M., Wood, M. J. A. & Turberfield, A. J. DNA cage delivery to mammalian cells. *ACS Nano* **5**, 5427–5432 (2011).
18. Lee, H. et al. Molecularly self-assembled nucleic acid nanoparticles for targeted in vivo siRNA delivery. *Nat. Nanotechnol.* **7**, 389–393 (2012).
19. Douglas, S. M., Bachelet, I. & Church, G. M. A logic-gated nanorobot for targeted transport of molecular payloads. *Science* **335**, 831–834 (2012).
20. Yang, L. et al. Extracellular vesicle-mediated delivery of circular RNA SCMH1 promotes functional recovery in rodent and nonhuman primate ischemic stroke models. *Circulation* **142**, 556–574 (2020).
21. Li, B. et al. FTO-dependent m(6)A modification of Plpp3 in circSCMH1-regulated vascular repair and functional recovery following stroke. *Nat. Commun.* **14**, 489 (2023).
22. Liang, L. et al. Single-particle tracking and modulation of cell entry pathways of a tetrahedral DNA nanostructure in live cells. *Angew. Chem. Int. Ed.* **53**, 7745–7750 (2014).
23. Zhou, M. et al. A DNA nanostructure-based neuroprotectant against neuronal apoptosis via inhibiting toll-like receptor 2 signaling pathway in acute ischemic stroke. *ACS Nano* **16**, 1456–1470 (2021).
24. Li, J. et al. Self-assembled multivalent DNA nanostructures for noninvasive intracellular delivery of immunostimulatory CpG oligonucleotides. *ACS Nano* **5**, 8783–8789 (2011).
25. Zong, W. et al. Miniature two-photon microscopy for enlarged field-of-view, multi-plane and long-term brain imaging. *Nat. Methods* **18**, 46–49 (2021).
26. Wang, L. et al. Rapid and ultrasensitive electromechanical detection of ions, biomolecules and SARS-CoV-2 RNA in unamplified samples. *Nat. Biomed. Eng.* **6**, 276–285 (2022).
27. Chen, L. L. The expanding regulatory mechanisms and cellular functions of circular RNAs. *Nat. Rev. Mol. Cell Biol.* **21**, 475–490 (2020).
28. Broto, M. et al. Nanozyme-catalysed CRISPR assay for preamplification-free detection of non-coding RNAs. *Nat. Nanotechnol.* **17**, 1120–1126 (2022).
29. Kristensen, L. S., Jakobsen, T., Hager, H. & Kjems, J. The emerging roles of circRNAs in cancer and oncology. *Nat. Rev. Clin. Oncol.* **19**, 188–206 (2022).
30. Lee, J. K., Kim, J. E., Sivula, M. & Strittmatter, S. M. Nogo receptor antagonism promotes stroke recovery by enhancing axonal plasticity. *J. Neurosci.* **24**, 6209–6217 (2004).
31. Clarkson, A. N., Huang, B. S., Macisaac, S. E., Mody, I. & Carmichael, S. T. Reducing excessive GABA-mediated tonic inhibition promotes functional recovery after stroke. *Nature* **468**, 305–309 (2010).
32. Zong, W. et al. Fast high-resolution miniature two-photon microscopy for brain imaging in freely behaving mice. *Nat. Methods* **14**, 713–719 (2017).
33. Wang, X. et al. Microbotic swarms for intracellular measurement with enhanced signal-to-noise ratio. *ACS Nano* **16**, 10824–10839 (2022).

Acknowledgements

We would like to thank Lin Yuan from Hunan University for providing the two-photon fluorophore. This work was supported by the National Natural Science Foundation of Distinguished Young Scholars grant 82025033 (to H.Y.), the Science and Technology Innovation 2030-Major Project of the Ministry of Science and Technology of China grant 2021ZD0202904/2021ZD0202900 (to H.Y.), the National Natural Science Foundation of China grants 82230115 (to H.Y.), 82473903 (to B.H.), 22174014 (to Y.Z.), 22304023 (to Z.Z.), 82373857 (to Y.Z.), and 82273914 (to Y.B.), the Natural Science Foundation Outstanding Youth Fund of Jiangsu Province grant BK20240175 (to B.H.), the Natural Science Foundation of Jiangsu Province grant BK20220802 (to Z.Z.), and the Fundamental Research Funds for the Central University grant 2242024RCB0026 (to B.H.).

Author contributions

H.Y., Y.J.Z., B.H., and Z.Z. conceived the study and designed the experiments. Z.Z. designed the TDF sensor. Z.Z. and N.L. conducted experiments on TDF sensor structure screening and characterization of specificity and sensitivity. Y.W. performed the cellular and molecular experiments. Y.W. and Z.Q.Z. established the mouse models of stroke. Z.Q.Z. performed two-photon imaging in awake animals. H.Y., B.H., and Z.Z. wrote the manuscript. H.Y., Y.J.Z., and Y.S. supervised the work. L.S., Y.B., and Y.Z. analyzed and checked the data. All authors contributed to the discussion.

Competing interests

The authors declare no competing interests.

Additional information

Supplementary information The online version contains supplementary material available at <https://doi.org/10.1038/s41467-024-55364-x>.

Correspondence and requests for materials should be addressed to Yuanjian Zhang or Honghong Yao.

Peer review information *Nature Communications* thanks Chunhai Fan, Biao Yan, and the other, anonymous, reviewer(s) for their contribution to the peer review of this work. A peer review file is available.

Reprints and permissions information is available at <http://www.nature.com/reprints>

Publisher's note Springer Nature remains neutral with regard to jurisdictional claims in published maps and institutional affiliations.

Open Access This article is licensed under a Creative Commons Attribution-NonCommercial-NoDerivatives 4.0 International License, which permits any non-commercial use, sharing, distribution and reproduction in any medium or format, as long as you give appropriate credit to the original author(s) and the source, provide a link to the Creative Commons licence, and indicate if you modified the licensed material. You do not have permission under this licence to share adapted material derived from this article or parts of it. The images or other third party material in this article are included in the article's Creative Commons licence, unless indicated otherwise in a credit line to the material. If material is not included in the article's Creative Commons licence and your intended use is not permitted by statutory regulation or exceeds the permitted use, you will need to obtain permission directly from the copyright holder. To view a copy of this licence, visit <http://creativecommons.org/licenses/by-nc-nd/4.0/>.

© The Author(s) 2024